remote sensing

MDPI

Article

High-Frequency Error Compensation for High-Resolution Satellite Stereo Images with Rough InSAR DSMs

Tao Huang [1], Deyin Liang [2], Zehua Cui [1], Shun Zhou [1], Xiaoyong Zhu [3], Hong Tang [1] and Hongbo Pan [1,*]

[1] School of Geosciences and Info-Physics, Central South University, #932 Lunan Road, Changsha 410083, China; huangtaosaf@csu.edu.cn (T.H.); czh1997@csu.edu.cn (Z.C.); zhoushuncsu@csu.edu.cn (S.Z.); 265001027@csu.edu.cn (H.T.)
[2] The Institute of Remote Sensing Satellites (IRSS) of the China Academy of Space Technology (CAST), Beijing 100830, China; liangdeyin_cast@outlook.com
[3] Land Satellite Remote Sensing Application Center, Ministry of Natural Resources of the People's Republic of China, Beijing 100048, China
* Correspondence: hongbopan@csu.edu.cn

Highlights

What are the main findings?

- A DSM-difference framework detects and compensates for high-frequency systematic errors in high-resolution satellite stereo imagery using a coarse-resolution InSAR DSM.
- Directional median elevation-difference profiles link object-space error detection to image-space compensation and subsequent DSM regeneration.

What are the implications of the main findings?

- The results support the use of a freely available InSAR DSM as an elevation reference for correcting coherent distortions in the investigated stereo pair.
- Transferring elevation corrections to image space improves directional consistency in the regenerated DSM and addresses distortions that remain after conventional adjustment.

Abstract

High-precision digital surface models (DSMs) derived from optical stereo satellite data are essential for various applications. However, DSMs generated from high-resolution satellite imagery often contain high-frequency errors associated with calibration inaccuracies and attitude jitter. This study exploits differences in the error characteristics of optical stereo-derived and interferometric synthetic aperture radar (InSAR)-derived DSMs to detect, model, and compensate for these errors. Dense bundle adjustment first corrects low-frequency errors in the optical stereo image pair. Elevation differences between the resulting optical DSM and the InSAR DSM are then analyzed to identify coherent directional error patterns. An object-space compensation model based on median elevation-difference profiles is established, and the elevation corrections are transferred to image space to compensate for the stereo imagery. Experiments using a single Ziyuan-3 02 (ZY-3 02) stereo pair showed reduced stripe patterns associated with residual high-frequency errors. Using the 30 m Copernicus GLO-30 DSM as the elevation reference, the flight-direction median-difference root mean square error (RMSE) decreased from 0.43 to 0.22 m (48.8%). The scan-direction RMSE decreased from 0.51 to 0.25 m (51.0%). Both reductions were relative to the Quadratic adjustment. The image-space residual RMSE calculated from the fitted error curves decreased from 0.132 to 0.032 pixels after compensation. Independent evaluation against ALOS World 3D 30 m (AW3D30) also showed reduced high-frequency

Check for updates

Academic Editor: Ana Cláudia Teodoro

Received: 24 September 2026
Revised: 2 November 2026
Accepted: 5 November 2026
Published: 7 November 2026

Copyright: © 2026 by the authors. Licensee MDPI, Basel, Switzerland. This article is an open access article distributed under the terms and conditions of the Creative Commons Attribution (CC BY) license.

systematic distortions. The flight- and scan-direction median-difference RMSEs decreased from 0.58 to 0.35 m (39.7%) and from 0.78 to 0.37 m (52.6%), respectively.

Keywords: digital surface models (DSMs); high-frequency errors; elevation difference; jitter; satellite images

1. Introduction

Digital surface models (DSMs) derived from high-resolution optical satellite imagery provide three-dimensional information for Earth observation and geospatial analysis. The accuracy and reliability of stereo-based DSM generation have therefore received sustained attention [1,2]. Global products such as ALOS World 3D 30 m (AW3D30), derived from the Advanced Land Observing Satellite (ALOS), support large-area applications [3]. High-resolution satellite-derived DSMs support scientific research and mapping, including applications in polar regions [4,5] and planetary mission planning and landing-site evaluation [6,7]. Ice, Cloud, and Land Elevation Satellite-2 (ICESat-2) laser altimetry has also been used to assess elevation biases and spatial variability in global elevation models [8]. DSMs additionally support topographic mapping, disaster assessment, environmental monitoring, and three-dimensional urban modeling [9,10].

Geometric errors limit the accuracy of DSMs generated from high-resolution satellite stereo imagery. Elevation estimates are sensitive to errors in stereo imaging geometry [11]. Attitude jitter and noise in attitude measurements can propagate into DSM elevations [12]. For stereo pairs with a small base-to-height ratio, even small image displacements can produce substantial elevation errors. Satellite attitude jitter can also distort and blur images, reducing their geometric and radiometric quality [13]. In this study, high-frequency errors refer to within-scene geometric variations that cannot be adequately represented by low-order adjustment models. This operational definition does not specify a fixed physical jitter frequency [14]. Slowly varying attitude-related errors can often be approximated using polynomial compensation models [15]. More complex errors associated with attitude variations and interior orientation distortions may remain after adjustment. Conventional methods commonly use polynomial models and ground control points to correct low-frequency errors [16,17]. More flexible approaches employ spline fitting [18] or high-resolution elevation references [19]. However, suitable control information and high-resolution elevation data are not always available.

Attitude-related errors can propagate into optical stereo-derived DSMs [20]. These DSMs may exhibit systematic directional errors, matching errors, and data voids [20]. InSAR-derived DSM errors have different dominant sources, including land cover, terrain, radar imaging geometry, and phase-unwrapping effects [21]. These differences in spatial error characteristics motivate the use of an InSAR DSM as an external elevation reference. In the proposed framework, the optical stereo-derived DSM is the target product, whereas the InSAR DSM is not assumed to be error-free. Comparing the co-registered DSMs can reveal coherent elevation-difference patterns that support geometric compensation [22,23]. Figure 1 illustrates the terrain and the corresponding inter-DSM differences. Panel (a) shows Copernicus DSM elevations. Panel (b) shows optical DSM elevations minus co-registered Copernicus elevations at corresponding locations on a common grid. Directional stripes may reflect residual optical geometric errors, whereas terrain-correlated patterns may contain contributions from both DSMs. The difference map therefore cannot be interpreted as the error of either product alone.

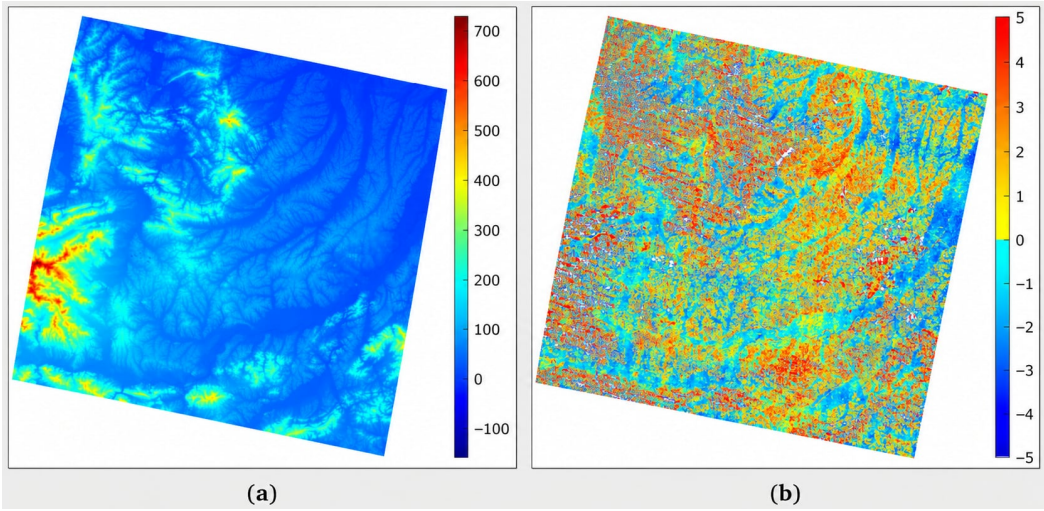


Figure 1. Terrain and inter-DSM elevation differences in the study area. (**a**) Copernicus GLO-30 elevations. (**b**) Optical stereo-derived DSM elevations minus co-registered Copernicus elevations. The differences contain contributions from both DSMs. Elevations and elevation differences are expressed in meters.

This study proposes a method for detecting and compensating for residual high-frequency errors in optical stereo imagery using a coarse, freely available InSAR DSM. The method addresses situations in which a high-resolution elevation reference is unavailable [19]. Directional median elevation-difference profiles characterize coherent variations along the flight and scan directions while reducing the influence of localized discrepancies. The resulting object-space corrections are propagated through rational function models to construct image-space compensation models. The corrected stereo images are then used to regenerate the DSM.

Section 2 reviews related work, Section 3 describes the method, and Section 4 presents the experiments. Sections 5 and 6 discuss the results and summarize the conclusions, respectively.

2. Related Work

Stereo satellite images acquired from different viewing angles allow elevations to be determined from matched tie points (TPs) and imaging geometry. Ground control points (GCPs) provide additional geometric constraints when available. Epipolar rectification aligns corresponding points along corresponding epipolar lines, reducing the matching search to one dimension. Residual geometric distortions can introduce disparities perpendicular to these lines and affect stereo matching. Errors in image correspondences or imaging geometry can then propagate into elevation estimates [24]. Low-order adjustment models reduce slowly varying geometric errors, but more rapid variations may remain [12]. Residual elevation errors may also arise from calibration inaccuracies, interior orientation distortions, matching errors, and processing artifacts [11].

The bias compensation model (BCM) [15], based on the rational function model (RFM), is widely used for geometric refinement of satellite imagery. Polynomial models correct image-space biases [25] using translation, drift, or affine terms [26]. However, low-order BCMs may not adequately represent complex nonlinear distortions. Zhou et al. used Sentinel-2 Level-1C imagery to extract GCPs for calibrating nonlinear distortions in Gaofen-6 (GF-6) wide-field imagery [27]. The approach depends on the quality and distribution of the reference control and does not directly address residual high-order elevation errors. Tong et al. developed a framework for jitter detection and compensation in the image and attitude domains [28]. Ye et al. [29] and Wang et al. [30] used multispectral imagery to estimate jitter

frequencies and amplitudes in the spatial or Fourier domain. Incomplete jitter modeling can nevertheless leave residual geometric errors [31]. Ye et al. further showed that image interpolation influences image-based jitter detection and compensation [32]. Zhang et al. developed a correction strategy for time-delay integration charge-coupled device (TDICCD) imagery by modeling jitter-induced distortions [33]. These methods principally address image-space distortions, while residual error propagation into stereo-derived elevations requires further consideration. Sutton et al. used Fourier analysis to estimate spacecraft motion associated with jitter-induced distortions, but correction remained challenging [11].

Inaccurate attitude measurements and unresolved attitude variations can introduce systematic errors into satellite RFMs. Such errors can affect the geometric positioning accuracy of high-resolution imagery [7,11]. More flexible compensation models include cubic splines [18], thin-plate smoothing splines [34], and local polynomials [35]. Their performance depends on the accuracy, availability, and spatial distribution of the control information. Attitude observations provide another basis for jitter estimation. Mo et al. used fast Fourier transform (FFT) analysis of gyroscope data to identify characteristic frequencies and construct a combined polynomial and trigonometric attitude model [36]. Wang et al. integrated high-frequency angular displacement measurements with star sensor observations to detect and compensate for jitter in Yaogan-26 imagery [37].

For a single stereo pair, limited viewing geometry can weaken the ability of self-calibrating dense bundle adjustment to recover rapidly varying errors [38]. In the configuration considered here, pitch-related errors may remain weakly constrained and propagate into elevation estimates. Recent line-by-line bundle-adjustment methods estimate scan-line-specific micro-vibrations using TPs and virtual ground control derived from freely available elevation data [39]. These methods require a modified rigorous imaging model and sufficient image correspondences. External elevation models offer an alternative when the objective is geometric compensation rather than independent recovery of time-dependent satellite attitude. Jacobsen discussed stereo-ray intersection and reference elevation models in relation to the limitations of satellite image orientation [40]. ICESat-2 observations have also been used to evaluate and improve global elevation models [8]. Spatially dense reference DSMs can support the detection of coherent errors by allowing localized discrepancies to be reduced through spatial aggregation [41]. Girod et al. developed the MicMac ASTER (MMASTER) framework for improving digital elevation models (DEMs) generated from Advanced Spaceborne Thermal Emission and Reflection Radiometer (ASTER) imagery [42]. The framework corrects jitter-induced cross-track parallax and reduces along-track artifacts in DEM comparisons. It improves the consistency of ASTER DEM time series, but is tailored to ASTER imaging geometry and processing. Loghin et al. used high-resolution elevation models to detect and estimate periodic geometric distortions in stereo imagery [19]. The limited availability of such references motivates further investigation of coarse-resolution DSMs for compensating residual errors in high-resolution optical stereo imagery [43].

3. Methods

The proposed method uses differences in the spatial error characteristics of optical stereo-derived and InSAR-derived DSMs to estimate image-space corrections. Figure 2 summarizes two stages: low-frequency error correction and residual high-frequency error detection and compensation. Dense bundle adjustment first updates the RFMs and estimates the object-space coordinates of the TPs. A DSM generated using the updated geometry is then co-registered with the InSAR DSM. Directional median elevation differences provide object-space correction estimates, which are transferred to image space through the RFMs. The combined flight- and scan-direction compensation models are used to resample the stereo images and regenerate the DSM.

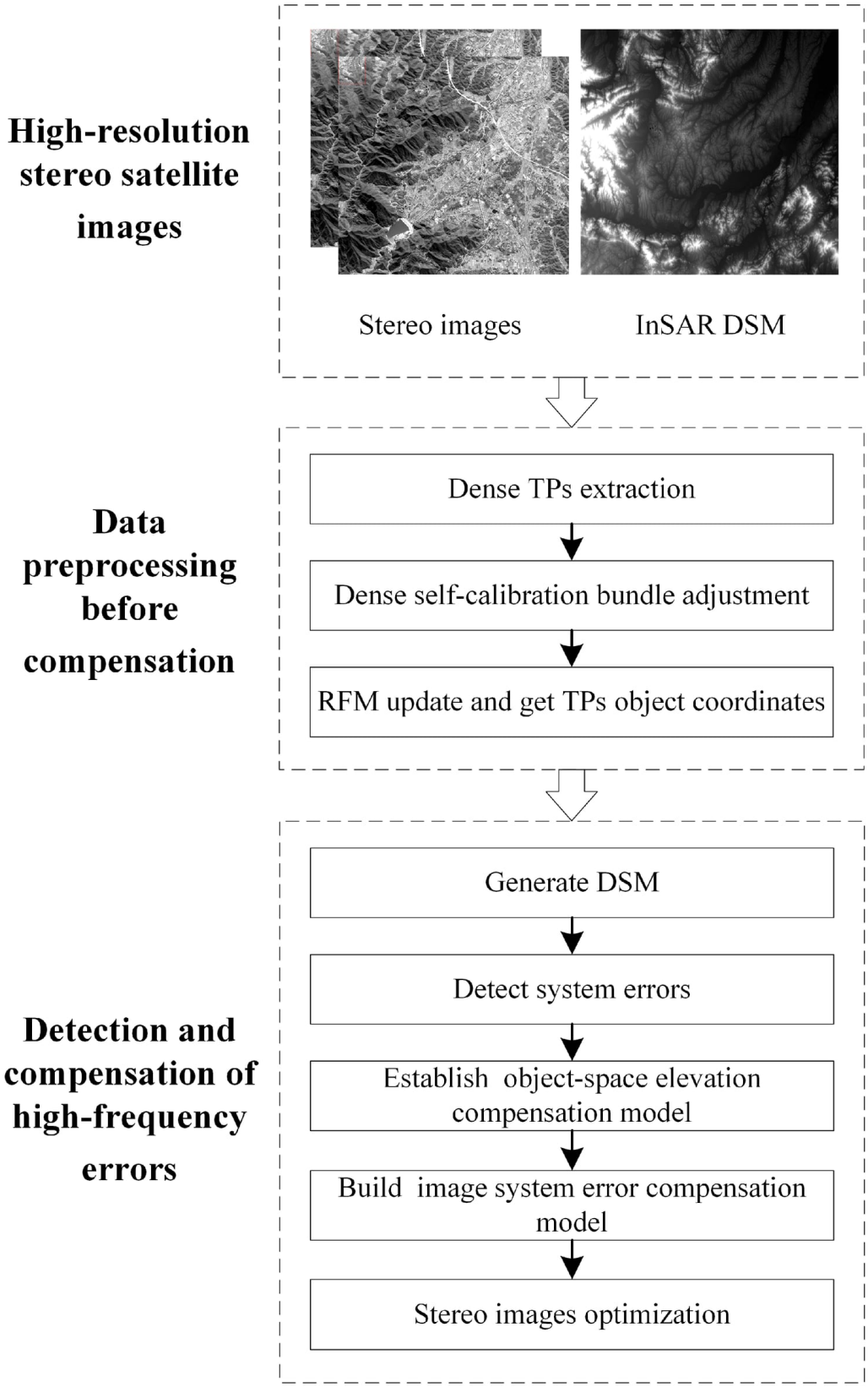


Figure 2. Workflow for high-frequency error detection and compensation using an InSAR DSM. Dense bundle adjustment refines the stereo geometry before DSM generation. Directional median elevation differences provide object-space corrections, which are transferred through the RFMs to construct image-space compensation models. Both directional models are applied during stereo-image resampling and subsequent DSM regeneration.

3.1. Correction of Low-Frequency Errors

Dense TPs are first extracted from the stereo image pair. The images are divided into blocks and geometrically corrected using the RFMs to support feature matching. The scale-invariant feature transform (SIFT) algorithm [44] is used for feature extraction and matching. Adaptive parameter local consistency (APLC) [45] is then used to remove mismatches.

Errors in exterior orientation parameters introduce systematic image-coordinate displacements [12]. When these displacements are approximately constant within a scene, they can be represented using a translation compensation model.

$$\begin{cases} \Delta s = a_0 \\ \Delta l = b_0 \end{cases} \tag{1}$$

Here, Δs and Δl are the correction values for the column and row coordinates in the image space, respectively, and a_0 and b_0 are the translation compensations for the column and row coordinates. If the errors in the satellite's exterior orientation parameters are not constant and vary linearly with time within the scope of a single scene, an affine model can be constructed to compensate for these errors:

$$\begin{cases} \Delta s = a_0 + a_1 \cdot l + a_2 \cdot s \\ \Delta l = b_0 + b_1 \cdot l + b_2 \cdot s \end{cases} \tag{2}$$

where s and l denote the image column (sample) and row (line) coordinates, respectively. The coefficients a_1 and a_2 describe the variation of Δs with l and s, respectively, while b_1 and b_2 describe the corresponding variation of Δl. For push-broom imagery, the line coordinate l is associated with acquisition time. When sample-dependent variations are negligible, the terms $a_2 s$ and $b_2 s$ can be omitted, reducing the affine model to a linear drift compensation model.

Dense self-calibrating bundle adjustment [38] uses the spatially distributed TPs to refine the imaging geometry. It can reduce low-order systematic errors, although more complex high-frequency components may remain. The updated RFMs are used to obtain TP object-space coordinates through forward intersection.

3.2. Detection of High-Frequency Errors

Semi-global matching (SGM) [46] generates the optical DSM using the RFMs refined by dense bundle adjustment. Horizontal offsets between the optical DSM and the InSAR DSM are estimated, and the InSAR DSM is co-registered to the optical DSM. Elevation differences are calculated as optical DSM elevations minus reference DSM elevations at corresponding locations. The difference map is rotated so that the row direction follows the satellite flight direction.

The planimetric coordinates of each TP are transformed into grid coordinates in the elevation-difference map. Both datasets use the same Universal Transverse Mercator (UTM) projection, allowing their coordinates to be related through the grid transformation parameters.

$$\begin{cases} r = \frac{t(4)\cdot X - t(1)\cdot Y - t(0)\cdot t(4) + t(1)\cdot t(3)}{t(2)\cdot t(4) - t(1)\cdot t(5)} \\ c = \frac{X - t(0) - t(2)\cdot r}{t(1)} \end{cases} \tag{3}$$

Here, (X,Y) represents the object-space planar coordinates of the TPs, $t(0)$ ... $t(5)$ represents the projection coordinate transformation parameters, and r and c denote the row and column coordinates of the TP in the DSM grid, respectively.

Median elevation differences are calculated for each row and column to reduce the influence of localized outliers. The resulting directional profiles are used to derive object-space elevation corrections, as illustrated in Figure 3.

$$\Delta h_c(r,c) = \Delta h_c(r) + \Delta h_c(c) \tag{4}$$

where $\Delta h_c(r)$ represents the median compensation function for the elevation difference in the flight direction and $\Delta h_c(c)$ represents the median compensation function in the scanning direction. Through object space compensation in both directions, $\Delta h_c(r,c)$ represents the elevation compensation value at the corresponding position (r,c).

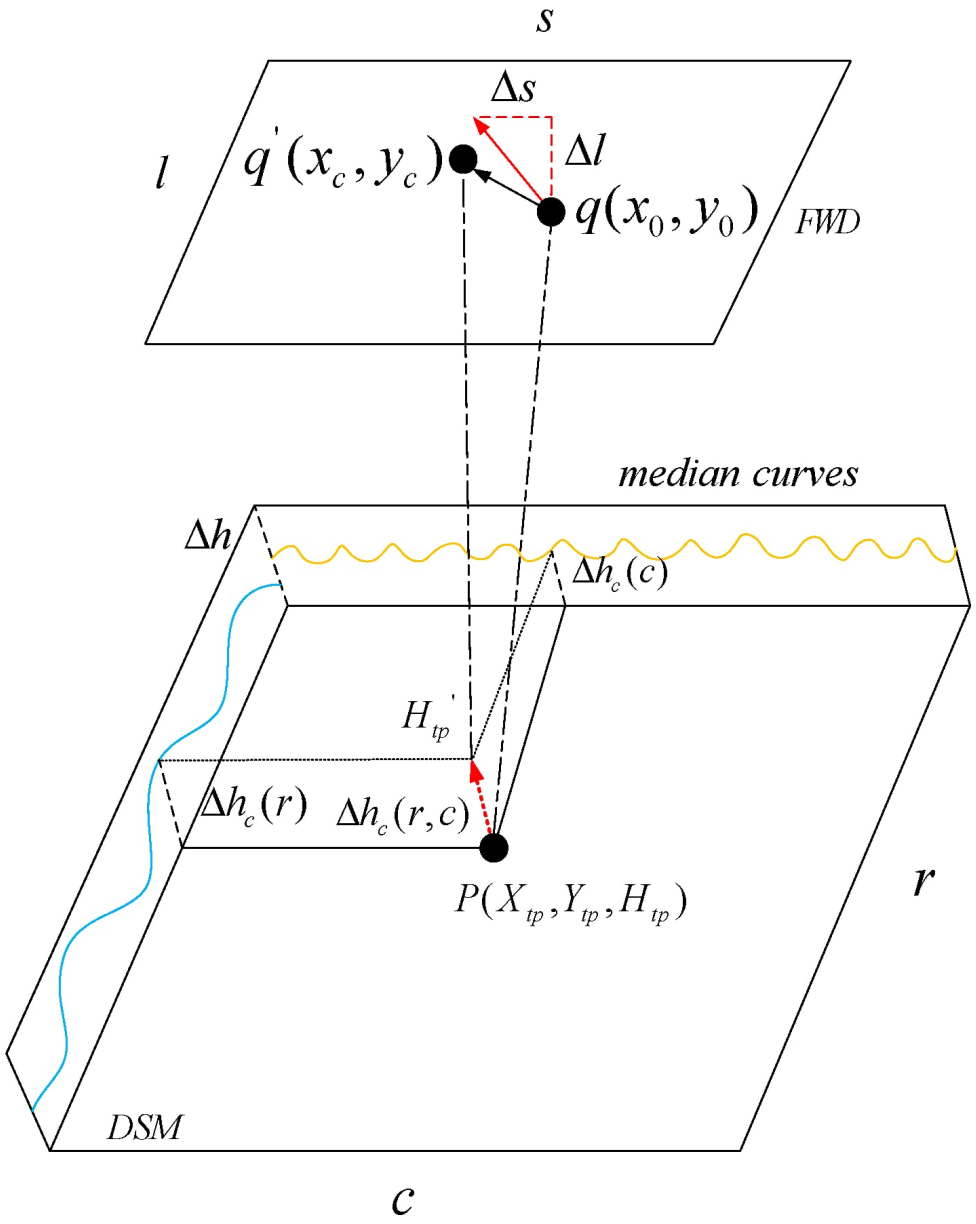


Figure 3. Detection and compensation diagram. P denotes the object-space point obtained by intersecting the viewing rays of corresponding image points; $\Delta h_c(r)$ and $\Delta h_c(c)$ denote the elevation corrections in the flight and scan directions, respectively; H' is the corrected elevation of P; q denotes the image coordinates obtained by back-projecting the object-space point at its original elevation; q' denotes the image coordinates obtained by back-projecting the object-space point with its corrected elevation; and Δs and Δl denote the sample- and line-coordinate differences between (q′) and (q), respectively.

3.3. Compensation of High-Frequency Errors

The object-space compensation model provides an elevation correction for each TP through interpolation, as illustrated in Figure 3. The correction is the negative of the interpolated median elevation difference, defined as optical DSM elevation minus refer-

ence DSM elevation. The corrected elevation is obtained by adding this correction to the original elevation.

$$H_{tp}{}' = H_{tp} + \Delta h_c(r,c) \tag{5}$$

Here, $\Delta h_c(r,c)$ represents the interpolated elevation compensation value at the corresponding position, H_{tp} represents the original elevation value of the TPs, and $H_{tp}{}'$ denotes the elevation value of the TPs after compensation.

Using the object-space planar coordinates of the TPs and the original elevation H_{tp}, as shown by point q in Figure 3, the original image point coordinates (x_0,y_0) in each image are calculated separately based on the RFM of the stereo pairs. Then, using the object-space planar coordinates of the TPs and the compensated elevation $H_{tp}{}'$, the elevation-compensated image point coordinates (x_c,y_c) are calculated for each of the two images via their respective RFMs. Finally, the difference between the original image point coordinates and the compensated coordinates is computed:

$$\begin{cases} \Delta x = x_c - x_o \\ \Delta y = y_c - y_o \end{cases} \tag{6}$$

The sample- and line-coordinate differences are modeled separately using cubic splines. Flight-direction models describe their variation with the image line coordinate, while scan-direction models describe their variation with the sample coordinate.

$$spl_x(l) = \sum_{j=0}^{m} P_j N_{j,3}(l) \tag{7}$$

Here, $spl_x(l)$ represents the fitted image residual value, l represents the image coordinate along the flight direction, P_j denotes the j-th spline coefficient, $N_{j,3}(l)$ denotes the j-th cubic B-spline basis function, j is the index of the B-spline basis function, and $m + 1$ is the total number of B-spline coefficients.

$$\begin{cases} N_{j,0}(l) = \begin{cases} 1, \ t_j \le l < t_{j+1} \\ 0, \ \text{else} \end{cases}, \\ N_{j,k}(l) = \frac{(l-t_j)}{t_{j+k}-t_j} N_{j,k-1}(l) + \frac{(t_{j+k+1}-l)}{t_{j+k+1}-t_{j+1}} N_{j+1,k-1}(l), \ k \ge 1 \end{cases} \tag{8}$$

where t_j denotes the j-th knot in the knot vector, and k denotes the degree of the B-spline basis function. For the cubic B-spline adopted in this study, $k = 3$. $N_{j,0}(l)$ is the zero-degree B-spline basis function, while higher-degree basis functions $N_{j,k}(l)$ are recursively calculated. If a denominator in the recursive expression is zero, the corresponding term is defined as zero. Given the knot vector, the B-spline basis functions are evaluated recursively using Equation (8). The sample- and line-coordinate differences are fitted separately using cubic splines to construct compensation models along the flight and scan directions. The fitted models are represented as piecewise cubic polynomials for subsequent image-space compensation.

The fitted flight-direction models provide pixelwise corrections for both image-coordinate components.

$$\begin{cases} \Delta s_e = spl_x(l) \\ \Delta l_e = spl_y(l) \end{cases} \tag{9}$$

where Δs_e and Δl_e represent pixel offset values for attitude jitter compensation, $spl_x(l)$ represents the fitted compensation value for Δx in the flight direction, and $spl_y(l)$ represents the fitted compensation value for Δy in the flight direction.

The scan-direction compensation models are formulated similarly.

$$\begin{cases} \Delta s_i = spl_x(s) \\ \Delta l_i = spl_y(s) \end{cases} \tag{10}$$

where Δs_i and Δl_i represent pixel offset values for intrinsic parameter compensation, $spl_x(s)$ represents the fitted compensation value for Δx in the scan direction, and $spl_y(s)$ represents the fitted compensation value for Δy in the scan direction.

$$\begin{cases} \Delta s = \Delta s_e + \Delta s_i \\ \Delta l = \Delta l_e + \Delta l_i \end{cases} \tag{11}$$

By applying compensation models in two directions, the final distortion correction Δs and Δl for each pixel in the image is obtained. For high-resolution imagery affected by jitter and artifacts, elevation compensation can be performed on a per-pixel basis. The method involves defining a fixed elevation plane and using the image point coordinates and the RFM to calculate the corresponding object-space point coordinates in the elevation plane. These coordinates are then reprojected into image space based on the object-space coordinates and the elevation-compensated imaging model, resulting in jitter-corrected image point coordinates. The corresponding pixel values are interpolated and used to replace the original pixel values. By applying this process to each pixel, a stereopair of high-resolution images with reduced high-frequency errors can be obtained.

4. Experiments and Analysis

4.1. Datasets

The experiment used a single stereo pair acquired by ZY-3 02, the second satellite in the ZY-3 series. The forward-looking (FWD) and nadir (NAD) images were acquired on 6 December 2016 at a spatial resolution of 2.5 m. The study area covers Ningxiang and its surroundings in Hunan, China, including plains and hilly terrain.

Two 30 m elevation datasets were used. Copernicus GLO-30 [21,47] provided the reference for high-frequency error detection and compensation modeling. It represents surface elevations, including buildings and vegetation. The reported absolute vertical accuracy is better than 4 m at the 90% linear-error level (LE90). The reported relative vertical accuracy is better than 4 m for slopes above 20% and better than 2 m for slopes below 20%. The reported absolute horizontal accuracy is better than 6 m at the 90% circular-error level (CE90) [48]. AW3D30 [49] was used only for independent evaluation and did not contribute to compensation-model estimation. The horizontal reference of Copernicus GLO-30 is the World Geodetic System 1984 (WGS84), and its vertical reference is the Earth Gravitational Model 2008 (EGM2008) geoid [50]. Before differencing, Copernicus orthometric heights were converted to WGS84 ellipsoidal heights by adding the corresponding EGM2008 geoid undulations. This matched the vertical reference of the generated optical DSM and the AW3D30 data used in this study.

4.2. High-Frequency Error Detection and Compensation

A total of 1,153,557 TPs were extracted from the FWD and NAD images. After dense bundle adjustment, most reprojection errors were within 0.2 pixels, as shown in Figure 4. Directional patterns remained in the residual distribution, indicating that the adjustment did not remove all spatially structured discrepancies.

The optical stereo-derived DSM was generated at a 30 m grid spacing to match the Copernicus reference. MicMac (version 1.0.beta14) [51] was used to co-register the two DSMs. Figure 5 shows the estimated horizontal offsets, which were mainly 0–15 m east–west and 5–20 m north–south. Elevation differences were then calculated between the co-registered DSMs. Grid cells with absolute differences greater than 5 m were excluded from the statistical analysis. Row- and column-wise median profiles provided object-space correction estimates, which were applied to the TP elevations and transferred to image space through the RFMs.

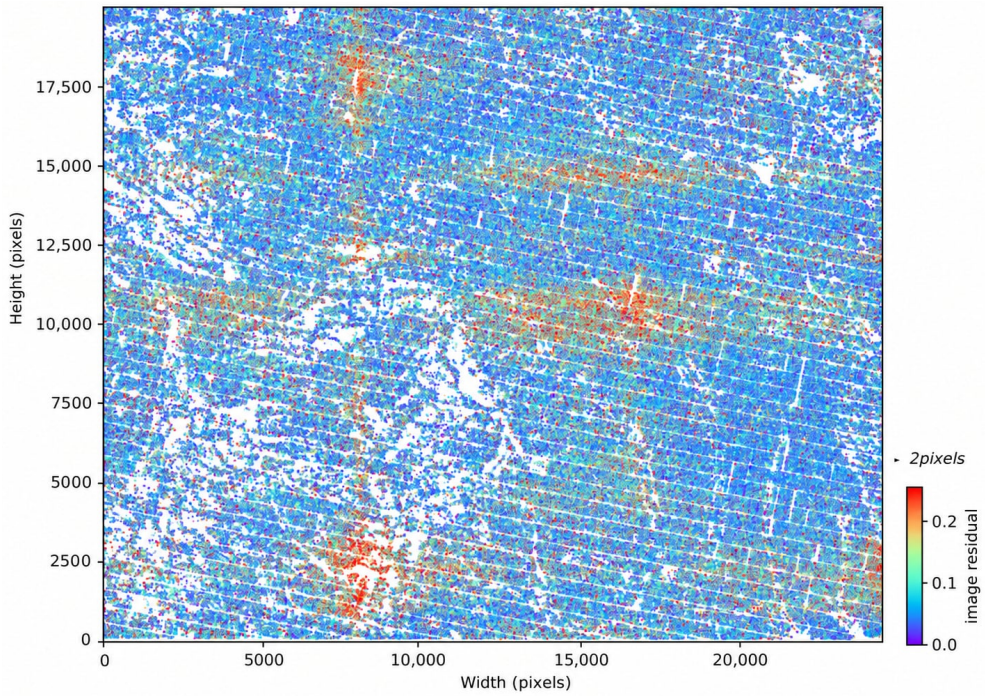


Figure 4. Reprojection error distributions of TPs in the NAD image after dense bundle adjustment.

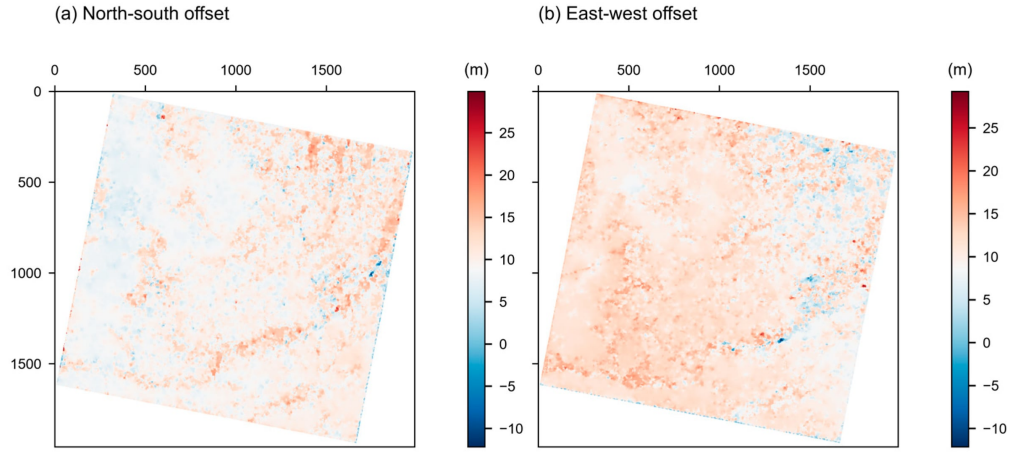


Figure 5. Estimated horizontal offsets between the optical stereo-derived and Copernicus DSMs during co-registration. (**a**) North–south offsets. (**b**) East–west offsets. Values are in meters.

Figures 6 and 7 show the fitted line-coordinate compensation models along the flight and scan directions, respectively. Blue points represent the calculated image-coordinate differences, and colored curves represent the cubic spline fits. Along the flight direction, FWD line-coordinate differences were mainly between −0.2 and 0.3 pixels. NAD differences were much smaller and generally followed an opposite trend. Along the scan direction, the FWD line-coordinate differences spanned approximately 0.5 pixels, while the NAD differences were again much smaller. Both sample- and line-coordinate components were retained in the compensation models, although Figures 6 and 7 display only the line components. These differences primarily reflect the response of each viewing geometry to the same elevation correction. The FWD camera observes at approximately 22° off nadir, whereas the NAD camera views approximately vertically. At fixed planimetric coordinates, elevation changes produce different image-coordinate displacements through the respective RFMs. The plotted corrections therefore reflect viewing-dependent height sensitivity rather than independent measurements of physical attitude jitter.

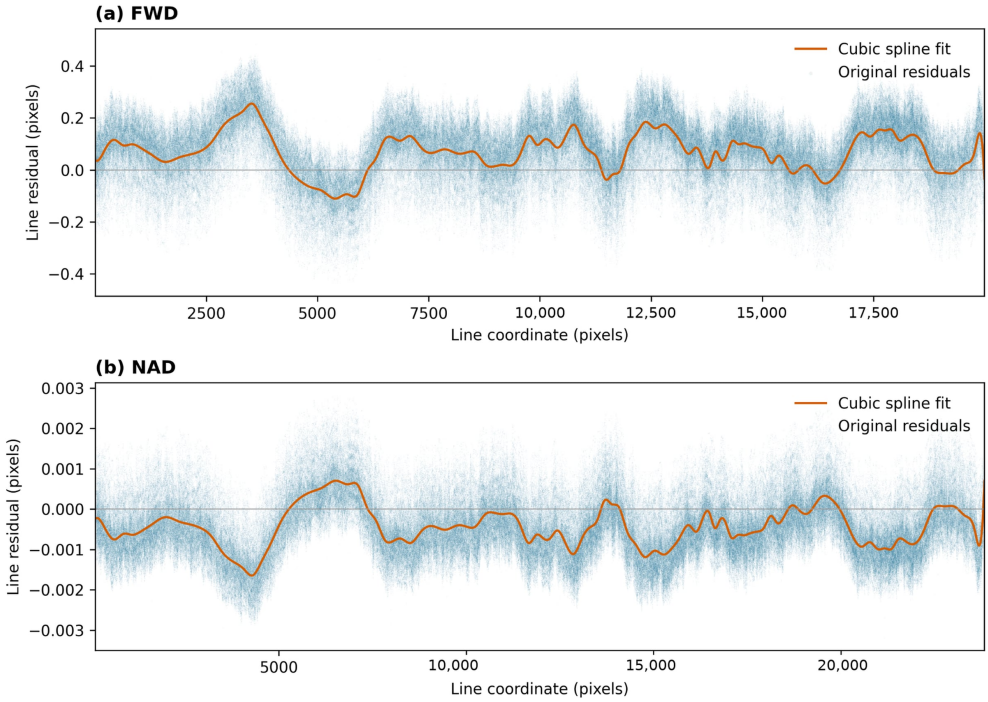


Figure 6. Image-space compensation models along the flight direction for the (**a**) FWD and (**b**) NAD images. Points show calculated line-coordinate differences as functions of the image line coordinate, and curves show the cubic spline fits. The panels use different vertical scales. Only the line-coordinate component is shown; both image-coordinate components were retained in compensation.

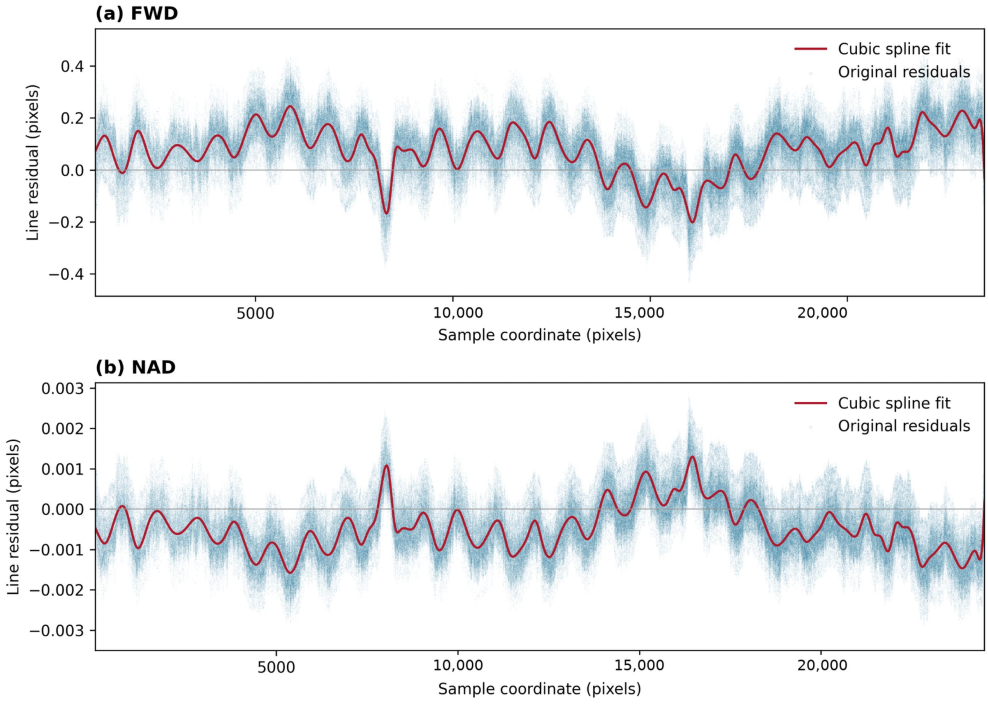


Figure 7. Image-space compensation models along the scan direction for the (**a**) FWD and (**b**) NAD images. Points show calculated line-coordinate differences as functions of the image sample coordinate, and curves show the cubic spline fits. The panels use different vertical scales. Only the line-coordinate component is shown; both image-coordinate components were retained in compensation.

Figure 8 compares the elevation differences before and after compensation. Grid cells with absolute elevation differences greater than 5 m were excluded to limit the influence of large local discrepancies. This filtering removed 5.43% of the valid pixels, retaining 94.57% for analysis,

and had little effect on the directional median profiles used for compensation modeling. The prominent stripe patterns weakened, and the median elevation-difference profiles showed smaller fluctuations in both the flight and scan directions. Localized discrepancies remained, indicating that compensation reduced coherent systematic distortions without eliminating all inter-DSM differences. After elevation compensation, the flight-direction median elevation differences narrowed from approximately −1.30–0.97 m to −0.55–0.13 m, while the scan-direction differences narrowed from approximately −1.24–1.49 m to −0.64–0.17 m. The peak-to-peak amplitudes decreased by approximately 70% in both directions.

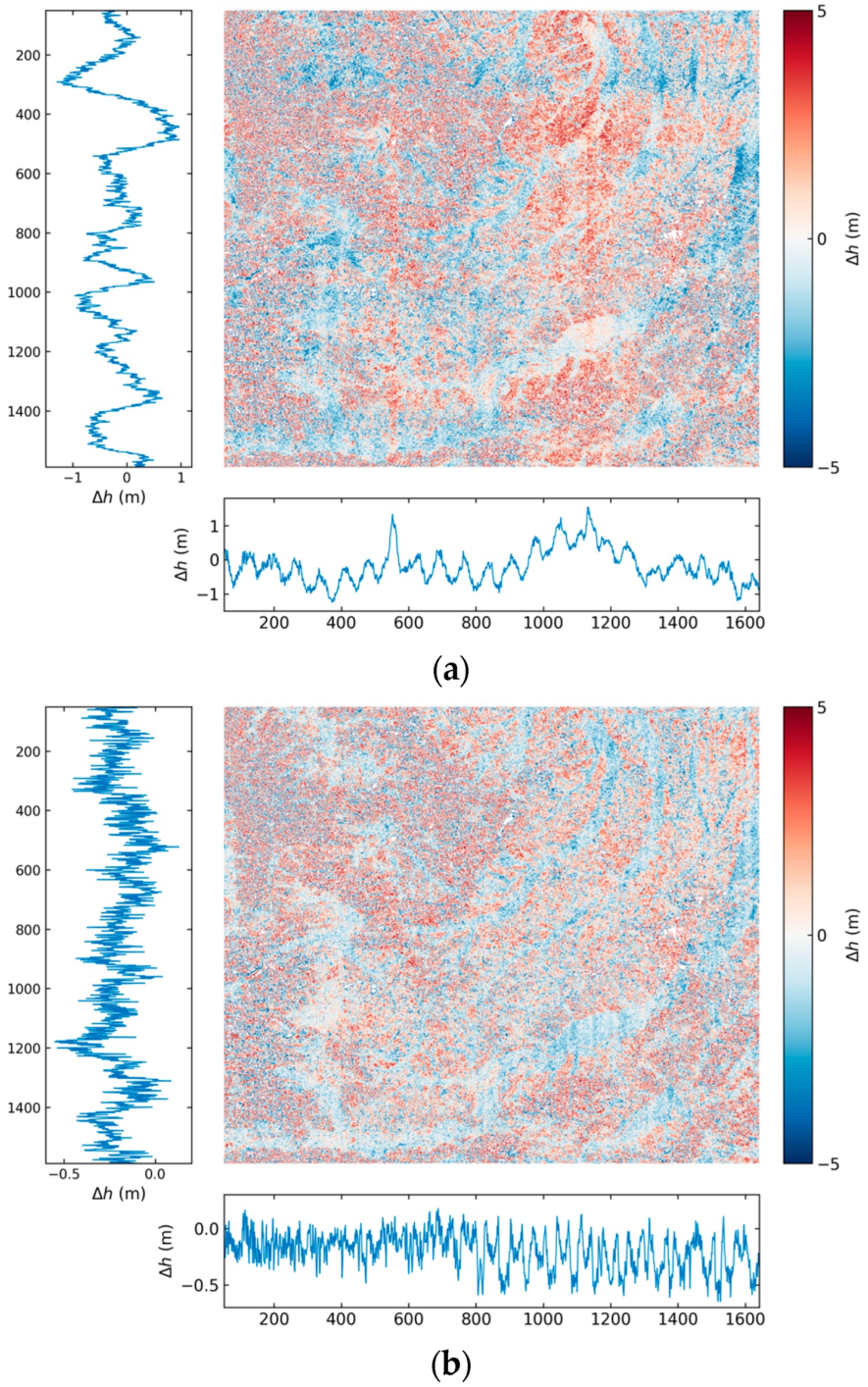


Figure 8. Elevation differences between the optical stereo-derived DSM and Copernicus GLO-30. (**a**) Before high-frequency compensation. (**b**) After compensation. Curves to the left and below each map show the flight- and scan-direction median differences, respectively.

Table 1 summarizes image-space residuals calculated from the fitted error curves before and after compensation. At each sampled position, the residual is the signed curve ordinate relative to the zero-error axis. These statistics describe modeled high-frequency errors and remaining curve-based residuals, rather than reprojection errors from a new bundle adjustment. The line- and sample-coordinate RMSEs decreased from 0.131 to 0.032 pixels and from 0.011 to 0.005 pixels, respectively. The combined two-dimensional RMSE decreased from 0.132 to 0.032 pixels, while the maximum two-dimensional residual magnitude decreased from 0.534 to 0.198 pixels.

Table 1. Image-space residual statistics before and after high-frequency compensation.

Compensation	ΔLine RMSE (Pixels)	ΔSample RMSE (Pixels)	RMSE (Pixels)	MAX (Pixels)
Uncompensated	0.131	0.011	0.132	0.534
Compensated	0.032	0.005	0.032	0.198

Regional differences remained visible after compensation in Figure 8b. Positive differences mainly occurred in mountainous and urban areas, while negative differences were more frequent in relatively flat regions. The flight-direction profile also retained abrupt variations near rows 390, 500, 750, 950, and 1200. These features may reflect residual optical geometric or matching errors, InSAR artifacts, and differences in spatial resolution or surface representation.

4.3. Comparative Evaluation and Independent Validation

The proposed method was compared with Translation, Affine, and Quadratic compensation models used in dense self-calibrating bundle adjustment [38]. Copernicus GLO-30 constrained the proposed compensation models, which were applied to the same stereo pair before DSM regeneration. The resulting DSMs were compared with Copernicus GLO-30 and independently evaluated against AW3D30.

Pixel-level DSM-difference RMSE was calculated from retained cell-wise elevation differences. Directional median RMSEs were calculated from the row- and column-wise median profiles relative to zero. Directional MAX values were the maximum absolute values of those profiles. Cells with absolute elevation differences greater than 5 m were excluded before calculating the statistics in Tables 2 and 3. These metrics quantify filtered agreement with the reference DSMs, not absolute elevation accuracy. Figure 9 compares the four methods against Copernicus GLO-30. The conventional adjustments produced similar stripe patterns and median-profile fluctuations. The proposed method reduced these patterns in both directions, although local discrepancies remained. Conventional-model DSM-difference RMSEs ranged from 1.94 to 1.98 m (Table 2). Relative to the Quadratic adjustment, the proposed method reduced this RMSE from 1.94 to 1.85 m (4.6%). Flight-direction median RMSE decreased from 0.43 to 0.22 m (48.8%), and scan-direction median RMSE decreased from 0.51 to 0.25 m (51.0%). The corresponding maximum absolute median differences decreased from 1.30 to 0.55 m and from 1.49 to 0.64 m, respectively.

Figure 10 shows the evaluation against AW3D30, which was not used to estimate the compensation models. The conventional adjustments retained similar directional patterns, while the proposed method reduced the broad fluctuations in both median profiles. Relative to the Quadratic adjustment, flight-direction median RMSE decreased from 0.58 to 0.35 m (39.7%). Scan-direction median RMSE decreased from 0.78 to 0.37 m (52.6%). The corresponding maximum absolute median differences decreased from 1.55 to 0.67 m and from 1.78 to 0.73 m (Table 3). Pixel-level DSM-difference RMSE decreased more modestly,

from 2.33 to 2.23 m (4.3%). This evaluation supports a reduction in coherent directional distortions beyond agreement with the DSM used for model estimation.

Table 2. DSM-difference statistics for the conventional models and proposed method compared with Copernicus GLO-30.

Method	DSM Difference RMSE (m)	Flight Direction RMSE (m)	Flight Direction MAX (m)	Scan Direction RMSE (m)	Scan Direction MAX (m)
Translation	1.98	0.45	1.27	0.53	1.61
Affine	1.97	0.44	1.26	0.50	1.60
Quadratic	1.94	0.43	1.30	0.51	1.49
Proposed	1.85	0.22	0.55	0.25	0.64

Table 3. Independent evaluation of DSM-difference statistics compared with AW3D30 for the conventional models and proposed method.

Method	DSM Difference RMSE (m)	Flight Direction RMSE (m)	Flight Direction MAX (m)	Scan Direction RMSE (m)	Scan Direction MAX (m)
Translation	2.34	0.60	1.43	0.80	1.84
Affine	2.34	0.58	1.45	0.79	1.84
Quadratic	2.33	0.58	1.55	0.78	1.78
Proposed	2.23	0.35	0.67	0.37	0.73

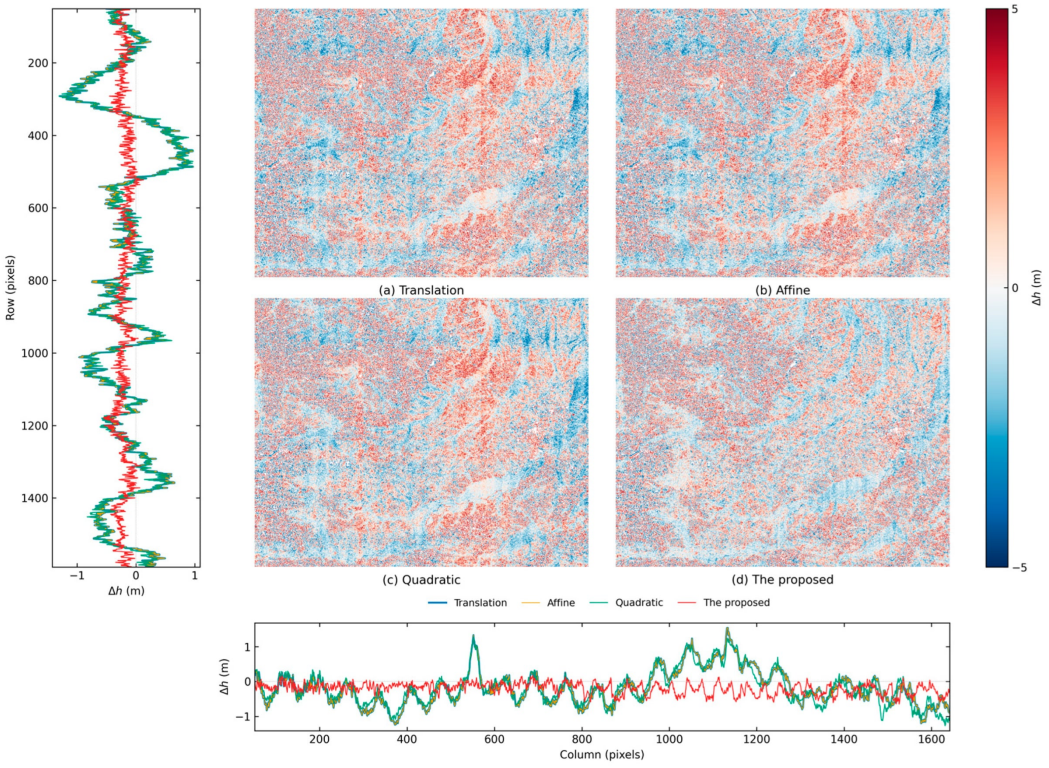


Figure 9. DSM elevation differences relative to Copernicus GLO-30 for the (**a**) Translation, (**b**) Affine, (**c**) Quadratic, and (**d**) Proposed methods. Profiles to the left and below the maps compare flight- and scan-direction median differences, respectively. Copernicus GLO-30 was also used to estimate the proposed compensation models.

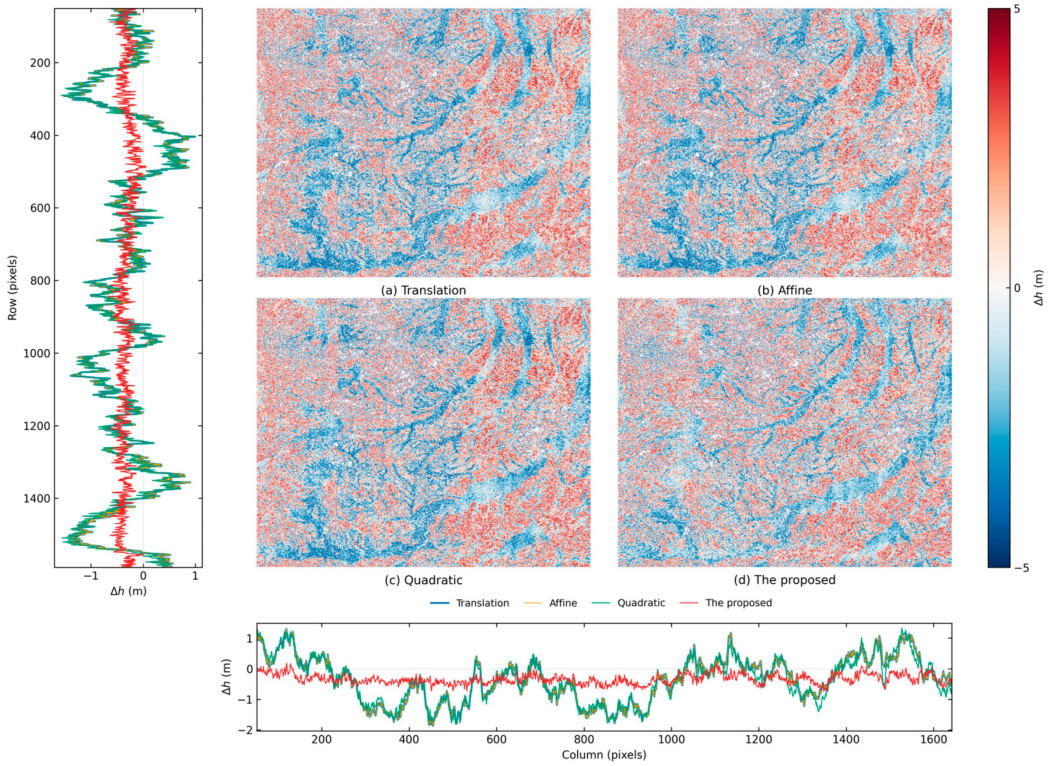


Figure 10. Independent evaluation of DSM elevation differences relative to AW3D30 for the (**a**) Translation, (**b**) Affine, (**c**) Quadratic, and (**d**) Proposed methods. Profiles to the left and below the maps compare flight- and scan-direction median differences, respectively. AW3D30 did not contribute to compensation-model estimation.

These results support the use of a coarse-resolution InSAR DSM to constrain coherent residual distortions in optical stereo imagery. The framework transfers elevation corrections to image space and regenerates the DSM. It provides an alternative when dense high-quality control data or accurate attitude observations are unavailable.

5. Discussion

The proposed method reduced directional median RMSEs more strongly than pixel-level DSM-difference RMSEs. This pattern is consistent with the suppression of coherent variations that low-order geometric models do not adequately represent [12,38,41]. However, the experiments do not independently recover satellite attitude or separate its contributions from other geometric errors. The fitted components should therefore be interpreted as empirical geometric corrections. The comparisons demonstrate an advantage over the tested conventional models for this stereo pair. Evaluation against AW3D30 strengthens this evidence because that dataset did not contribute to model estimation. Nevertheless, both reference products are coarse-resolution DSMs with terrain- and land-cover-dependent uncertainties.

The required reference resolution depends on the spatial wavelength of the error being estimated, rather than directly on the optical image pixel size. For sufficiently long-wavelength variations, a 30 m DSM can provide a suitable reference for identifying coherent patterns. Wavelengths greater than 120 m satisfy a conservative criterion of more than four 30 m sampling intervals per cycle. The principal variations observed in this study occurred at approximately 3–25 km, substantially exceeding that sampling scale. Interpolation can provide reference elevations at denser computational locations, but it adds no new terrain information to the original DSM. Short-wavelength error detection therefore remains limited by the reference information content, noise, and terrain complexity. A higher-resolution

reference is preferable when error wavelengths approach the scale of terrain variations unresolved by the coarse DSM [19].

The elevation-difference map contains contributions from both DSMs. Vegetation, buildings, steep terrain, and InSAR imaging and processing effects can introduce localized or terrain-dependent discrepancies [21,48]. In vegetated areas, X-band interferometric elevations are influenced by the radar scattering phase center, and GLO-30 vegetation biases vary with canopy height [52]. Row- and column-wise medians reduce the influence of localized outliers, but retain coherent variations that may originate in either product. This distinction is particularly relevant in areas with vegetation and complex terrain [21,48]. Large-scale or spatially coherent reference artifacts may bias the median profiles and propagate into the compensation models. Masking differences greater than 5 m removes pronounced local discrepancies but does not eliminate systematic biases in either DSM. Shared biases may also cancel in the difference map and remain undetected. The method therefore relies on sufficiently different dominant spatial error patterns in the optical and InSAR DSMs. Substantial overlap between these patterns may reduce the reliability of the estimated corrections.

6. Conclusions

This study developed a method that uses a coarse-resolution InSAR DSM to detect and compensate for residual high-frequency systematic errors in high-resolution satellite stereo imagery by linking directional median elevation differences with image-space corrections. For a single ZY-3 02 stereo pair over Ningxiang, Hunan, the method reduced flight- and scan-direction median RMSEs from 0.43 to 0.22 m and from 0.51 to 0.25 m against Copernicus GLO-30, respectively, relative to the Quadratic adjustment. Independent evaluation against AW3D30 showed corresponding reductions from 0.58 to 0.35 m and from 0.78 to 0.37 m. These results demonstrate reduced coherent directional distortions in the tested stereo pair, although improvements in pixel-level DSM agreement were more modest.

The method estimates empirical geometric corrections rather than independently identifying physical error sources, and its performance depends on the reference DSM and the spatial characteristics of the errors. Future work will assess its applicability across multiple sensors and acquisition periods using independent validation data.

Author Contributions: Conceptualization, T.H. and D.L.; methodology, T.H. and Z.C.; validation, T.H. and H.T.; formal analysis, T.H. and Z.C.; investigation, T.H.; resources, H.P. and D.L.; data curation, H.T. and S.Z.; writing—original draft preparation, T.H.; writing—review and editing, H.P., X.Z. and D.L.; visualization, Z.C.; supervision, H.P. and D.L.; project administration, H.P., X.Z. and D.L.; funding acquisition, H.P. All authors have read and agreed to the published version of the manuscript.

Funding: This research was funded by the National Natural Science Foundation of China (Grant No. 42271410) and the Second Batch of the Civil Aerospace Technology Pre-Research Project (Project No. D030104). The APC was funded by Hongbo Pan.

Data Availability Statement: The Copernicus GLO-30 DSM used for compensation modeling is publicly available through the Copernicus Data Space Ecosystem (https://portal.opentopography.org/datasetMetadata?otCollectionID=OT.032021.4326.1, accessed on 4 November 2026). The AW3D30 DSM used for independent evaluation is freely available from JAXA after user registration (https://www.eorc.jaxa.jp/ALOS/en/aw3d30/registration.htm, accessed on 4 November 2026).

Acknowledgments: The authors would like to express their gratitude to everyone who contributed to this article.

Conflicts of Interest: The authors declare no conflicts of interest.

Abbreviations

The following abbreviations are used in this manuscript:

DSM	Digital Surface Model
InSAR	Interferometric Synthetic Aperture Radar
RFM	Rational Function Model
BCM	Bias Compensation Model
GCP	Ground Control Point
TPs	Tie Points
BA	Bundle Adjustment
SGM	Semi-Global Matching
SIFT	Scale-Invariant Feature Transform
APLC	Adaptive Parameter Local Consistency
FWD	Forward-looking Image
NAD	Nadir Image
FFT	Fast Fourier Transform
RMSE	Root Mean Square Error
MAX	Maximum residual magnitude or maximum absolute median difference
RPC	Rational Polynomial Coefficient
AW3D30	Advanced Land Observing Satellite World 3D 30-m Resolution DSM
VHR	Very High Resolution
TDICCD	Time Delay Integration Charge-Coupled Device
GLO-30	Global 30 m Copernicus Digital Elevation Model
ALOS	Advanced Land Observing Satellite
ASTER	Advanced Spaceborne Thermal Emission and Reflection Radiometer
DEM	Digital Elevation Model
EGM2008	Earth Gravitational Model 2008
UTM	Universal Transverse Mercator
WGS84	World Geodetic System 1984
LE90	Linear Error at the 90% Confidence Level
CE90	Circular Error at the 90% Confidence Level
ICESat-2	Ice, Cloud, and land Elevation Satellite-2
MMASTER	MicMac ASTER
JAXA	Japan Aerospace Exploration Agency
GF-6	Gaofen-6
ZY-3 02	Ziyuan-3 02

References

1. Qin, R. A critical analysis of satellite stereo pairs for digital surface model generation and a matching quality prediction model. *ISPRS J. Photogramm. Remote Sens.* **2019**, *154*, 139–150. [CrossRef]
2. Yin, T.; Montesano, P.M.; Cook, B.D.; Chavanon, E.; Neigh, C.S.; Shean, D.; Peng, D.; Lauret, N.; Mkaouar, A.; Morton, D.C. Modeling forest canopy surface retrievals using very high-resolution spaceborne stereogrammetry: (I) methods and comparisons with actual data. *Remote Sens. Environ.* **2023**, *298*, 113825. [CrossRef]
3. Tadono, T.; Nagai, H.; Ishida, H.; Oda, F.; Naito, S.; Minakawa, K.; Iwamoto, H. Generation of the 30 M-mesh global digital surface model by ALOS PRISM. *Int. Arch. Photogramm. Remote Sens. Spat. Inf. Sci.* **2016**, *41*, 157–162. [CrossRef]
4. Takaku, J.; Tadono, T.; Tsutsui, K. Generation of High Resolution Global DSM from ALOS PRISM. *Int. Arch. Photogramm. Remote Sens. Spat. Inf. Sci.* **2014**, *XL-4*, 243–248. [CrossRef]
5. Porter, C.; Howat, I.; Noh, M.-J.; Husby, E.; Khuvis, S.; Danish, E.; Tomko, K.; Gardiner, J.; Negrete, A.; Yadav, B. *ArcticDEM–Strips*; Version 4.1; Harvard Dataverse: Massachusetts, MA, USA, 2022; Volume 1.
6. Golombek, M.; Grant, J.; Kipp, D.; Vasavada, A.; Kirk, R.; Fergason, R.; Bellutta, P.; Calef, F.; Larsen, K.; Katayama, Y. Selection of the Mars Science Laboratory landing site. *Space Sci. Rev.* **2012**, *170*, 641–737. [CrossRef]
7. Kirk, R.L.; Howington-Kraus, E.; Rosiek, M.R.; Anderson, J.A.; Archinal, B.A.; Becker, K.J.; Cook, D.; Galuszka, D.M.; Geissler, P.E.; Hare, T.M. Ultrahigh resolution topographic mapping of Mars with MRO HiRISE stereo images: Meter-scale slopes of candidate Phoenix landing sites. *J. Geophys. Res. Planets* **2008**, *113*, E00A24. [CrossRef]
8. Jacobsen, K.; Büyüksalih, G.; Gazioglu, C. Accuracy Analysis and Improvement of Worldwide Elevation Models by ICESat-2 data. *ISPRS Open J. Photogramm. Remote Sens.* **2026**, *19*, 100115. [CrossRef]
9. Toutin, T.; Schmitt, C.V.; Wang, H. Impact of no GCP on elevation extraction from WorldView stereo data. *ISPRS J. Photogramm. Remote Sens.* **2012**, *72*, 73–79. [CrossRef]

10. Holland, D.A.; Boyd, D.S.; Marshall, P. Updating topographic mapping in Great Britain using imagery from high-resolution satellite sensors. *ISPRS J. Photogramm. Remote Sens.* **2006**, *60*, 212–223. [CrossRef]
11. Sutton, S.; Boyd, A.; Kirk, R.L.; Cook, D.; Backer, J.; Fennema, A.; Heyd, R.; McEwen, A.; Mirchandani, S. Correcting spacecraft jitter in HiRISE images. In *Planetary Remote Sensing and Mapping*; CRC Press: Boca Raton, FL, USA, 2018; pp. 91–106.
12. Pan, H.; Tao, C.; Zou, Z. Precise georeferencing using the rigorous sensor model and rational function model for ZiYuan-3 strip scenes with minimum control. *ISPRS J. Photogramm. Remote Sens.* **2016**, *119*, 259–266. [CrossRef]
13. Akira, I. Detection and Estimation Satellite Attitude Jitter Using Remote Sensing Imagery. In *Advances in Spacecraft Technologies*; Jason, H., Ed.; IntechOpen: Rijeka, Croatia, 2011; Chapter 13.
14. Wang, M.; Zhu, Y.; Fan, C. Development of Platform Jitter Geometric Analysis and Processing for High-Resolution Optical Satellite Imagery. *Wuhan Daxue Xuebao (Xinxi Kexue Ban)/Geomat. Inf. Sci. Wuhan Univ.* **2018**, *43*, 1899–1908. [CrossRef]
15. Fraser, C.S.; Hanley, H.B. Bias compensation in rational functions for IKONOS satellite imagery. *Photogramm. Eng. Remote Sens.* **2003**, *69*, 53–57. [CrossRef]
16. Barazzetti, L.; Roncoroni, F.; Brumana, R.; Previtali, M. Georeferencing accuracy analysis of a single worldview-3 image collected over milan. *Int. Arch. Photogramm. Remote Sens. Spat. Inf. Sci.* **2016**, *41*, 429–434. [CrossRef]
17. Hu, F.; Gao, X.; Li, G.; Li, M. DEM extraction from worldview-3 stereo-images and accuracy evaluation. *Int. Arch. Photogramm. Remote Sens. Spat. Inf. Sci.* **2016**, *41*, 327–332. [CrossRef]
18. Cao, J.; Fu, J.; Yuan, X.; Gong, J. Nonlinear bias compensation of ZiYuan-3 satellite imagery with cubic splines. *ISPRS J. Photogramm. Remote Sens.* **2017**, *133*, 174–185. [CrossRef]
19. Loghin, A.-M.; Otepka-Schremmer, J.; Ressl, C.; Pfeifer, N. Improvement of VHR Satellite Image Geometry with High Resolution Elevation Models. *Remote Sens.* **2022**, *14*, 2303. [CrossRef]
20. Hoja, D.; Reinartz, P.; Schroeder, M. Comparison of DEM generation and combination methods using high resolution optical stereo imagery and interferometric SAR data. *Rev. Fr. Photogrammétrie Télédétect.* **2007**, *2006*, 89–94.
21. Rizzoli, P.; Martone, M.; Gonzalez, C.; Wecklich, C.; Borla Tridon, D.; Bräutigam, B.; Bachmann, M.; Schulze, D.; Fritz, T.; Huber, M.; et al. Generation and performance assessment of the global TanDEM-X digital elevation model. *ISPRS J. Photogramm. Remote Sens.* **2017**, *132*, 119–139. [CrossRef]
22. Pham, H.T.; Marshall, L.; Johnson, F.; Sharma, A. A method for combining SRTM DEM and ASTER GDEM2 to improve topography estimation in regions without reference data. *Remote Sens. Environ.* **2018**, *210*, 229–241. [CrossRef]
23. Guan, L.; Pan, H.; Zou, S.; Hu, J.; Zhu, X.; Zhou, P. The impact of horizontal errors on the accuracy of freely available Digital Elevation Models (DEMs). *Int. J. Remote Sens.* **2020**, *41*, 7383–7399. [CrossRef]
24. Kirk, R.L.; Howington-Kraus, E.; Redding, B.; Galuszka, D.; Hare, T.M.; Archinal, B.A.; Soderblom, L.A.; Barrett, J.M. High-resolution topomapping of candidate MER landing sites with Mars Orbiter Camera narrow-angle images. *J. Geophys. Res. Planets* **2003**, *108*, 8098. [CrossRef]
25. Xiong, Z.; Zhang, Y. A generic method for RPC refinement using ground control information. *Photogramm. Eng. Remote Sens.* **2009**, *75*, 1083–1092. [CrossRef]
26. Li, C.; Shen, Y.; Li, B.; Qiao, G.; Liu, S.; Wang, W.; Tong, X. An improved geopositioning model of QuickBird high resolution satellite imagery by compensating spatial correlated errors. *ISPRS J. Photogramm. Remote Sens.* **2014**, *96*, 12–19. [CrossRef]
27. Zhou, S.; Pan, H.; Huang, T.; Zhou, P. High Accuracy Georeferencing of GF-6 Wide Field of View Scenes Toward Analysis Ready Data. *IEEE Trans. Geosci. Remote Sens.* **2023**, *61*, 1–12. [CrossRef]
28. Tong, X.; Ye, Z.; Xu, Y.; Tang, X.; Liu, S.; Li, L.; Xie, H.; Wang, F.; Li, T.; Hong, Z. Framework of Jitter Detection and Compensation for High Resolution Satellites. *Remote Sens.* **2014**, *6*, 3944–3964. [CrossRef]
29. Ye, Z.; Xu, Y.; Tong, X.; Zheng, S.; Zhang, H.; Xie, H.; Stilla, U. Estimation and analysis of along-track attitude jitter of ZiYuan-3 satellite based on relative residuals of tri-band multispectral imagery. *ISPRS J. Photogramm. Remote Sens.* **2019**, *158*, 188–200. [CrossRef]
30. Wang, M.; Zhu, Y.; Pan, J.; Yang, B.; Zhu, Q. Satellite jitter detection and compensation using multispectral imagery. *Remote Sens. Lett.* **2016**, *7*, 513–522. [CrossRef]
31. Pan, H.; Zou, Z.; Zhang, G.; Zhu, X.; Tang, X. A Penalized Spline-Based Attitude Model for High-Resolution Satellite Imagery. *IEEE Trans. Geosci. Remote Sens.* **2016**, *54*, 1849–1859. [CrossRef]
32. Ye, Z.; Xu, Y.; Wei, C.; Tong, X.; Stilla, U. Influence of image interpolation on imagery-based detection and compensation of satellite jitter. *ISPRS Ann. Photogramm. Remote Sens. Spat. Inf. Sci.* **2020**, *1*, 157–163. [CrossRef]
33. Zhang, H.; Xie, B.; Liu, S.; Ding, R.; Ye, Z.; Tong, X. Detection and correction of jitter effect for satellite TDICCD imagery. *Int. Arch. Photogramm. Remote Sens. Spat. Inf. Sci.* **2022**, *43*, 79–84. [CrossRef]
34. Shen, X.; Liu, B.; Li, Q.-Q. Correcting bias in the rational polynomial coefficients of satellite imagery using thin-plate smoothing splines. *ISPRS J. Photogramm. Remote Sens.* **2017**, *125*, 125–131. [CrossRef]
35. Shen, X.; Li, Q.; Wu, G.; Zhu, J. Bias compensation for rational polynomial coefficients of high-resolution satellite imagery by local polynomial modeling. *Remote Sens.* **2017**, *9*, 200. [CrossRef]

36. Mo, F.; Tang, X.; Xie, J.; Yan, C. An Attitude Modelling Method Based on the Inherent Frequency of A Satellite Platform. *Int. Arch. Photogramm. Remote Sens. Spat. Inf. Sci.* **2017**, *XLII-1/W1*, 29–33. [CrossRef]
37. Wang, M.; Fan, C.; Pan, J.; Jin, S.; Chang, X. Image jitter detection and compensation using a high-frequency angular displacement method for Yaogan-26 remote sensing satellite. *ISPRS J. Photogramm. Remote Sens.* **2017**, *130*, 32–43. [CrossRef]
38. Pan, H.; Huang, T.; Zhou, P.; Cui, Z. Self-calibration dense bundle adjustment of multi-view Worldview-3 basic images. *ISPRS J. Photogramm. Remote Sens.* **2021**, *176*, 127–138. [CrossRef]
39. Xu, S.; Cao, J.; Huang, P.; Yuan, Y.; Fang, Y.; Chen, H.; Wu, M.; Long, T. Microvibration detection and compensation for SDGSAT-1 based on line-by-line bundle adjustment. *Remote Sens. Environ.* **2026**, *335*, 115245. [CrossRef]
40. Jacobsen, K. Problems and Limitations of Satellite Image Orientation for Determination of Height Models. *ISPRS-Int. Arch. Photogramm. Remote Sens. Spat. Inf. Sci.* **2017**, *42*, 257–264. [CrossRef]
41. Jacobsen, K. Systematic Geometric Image Errors of Very High Resolution Optical Satellites. *ISPRS-Int. Arch. Photogramm. Remote Sens. Spat. Inf. Sci.* **2018**, *XLII-1*, 233–238. [CrossRef]
42. Girod, L.; Nuth, C.; Kääb, A.; McNabb, R.; Galland, O. MMASTER: Improved ASTER DEMs for elevation change monitoring. *Remote Sens.* **2017**, *9*, 704. [CrossRef]
43. Takaku, J.; Tadono, T. High resolution dsm generation from alos prism-processing status and influence of attitude fluctuation. In Proceedings of the 2010 IEEE International Geoscience and Remote Sensing Symposium, Honolulu, HI, USA, 25–30 July 2010; pp. 4228–4231.
44. Lowe, D.G. Distinctive Image Features from Scale-Invariant Keypoints. *Int. J. Comput. Vis.* **2004**, *60*, 91–110. [CrossRef]
45. Huang, T.; Pan, H.; Zhou, N. Adaptive parameter local consistency automatic outlier removal algorithm for area-based matching. *ISPRS Ann. Photogramm. Remote Sens. Spat. Inf. Sci.* **2024**, *X-1-2024*, 99–106. [CrossRef]
46. Hirschmuller, H. Stereo processing by semiglobal matching and mutual information. *IEEE Trans. Pattern Anal. Mach. Intell.* **2007**, *30*, 328–341. [CrossRef] [PubMed]
47. Bielski, C.; López-Vázquez, C.; Grohmann, C.H.; Guth, P.L.; Hawker, L.; Gesch, D.; Trevisani, S.; Herrera-Cruz, V.; Riazanoff, S.; Corseaux, A.; et al. Novel Approach for Ranking DEMs: Copernicus DEM Improves One Arc Second Open Global Topography. *IEEE Trans. Geosci. Remote Sens.* **2024**, *62*, 1–22. [CrossRef]
48. Trevisani, S.; Skrypitsyna, T.N.; Florinsky, I.V. Global digital elevation models for terrain morphology analysis in mountain environments: Insights on Copernicus GLO-30 and ALOS AW3D30 for a large Alpine area. *Environ. Earth Sci.* **2023**, *82*, 198. [CrossRef]
49. Tadono, T.; Takaku, J.; Tsutsui, K.; Oda, F.; Nagai, H. Status of "ALOS World 3D (AW3D)" global DSM generation. In Proceedings of the 2015 IEEE International Geoscience and Remote Sensing Symposium (IGARSS), Milan, Italy, 13–18 July 2015; pp. 3822–3825.
50. Pavlis, N.K.; Holmes, S.A.; Kenyon, S.C.; Factor, J.K. The development and evaluation of the Earth Gravitational Model 2008 (EGM2008). *J. Geophys. Res. Solid Earth* **2012**, *117*, B04406. [CrossRef]
51. Rupnik, E.; Daakir, M.; Pierrot Deseilligny, M. MicMac–A free, open-source solution for photogrammetry. *Open Geospat. Data Softw. Stand.* **2017**, *2*, 1–9. [CrossRef]
52. Simard, M.; Denbina, M.; Marshak, C.; Neumann, M. A Global Evaluation of Radar-Derived Digital Elevation Models: SRTM, NASADEM, and GLO-30. *J. Geophys. Res. Biogeosciences* **2024**, *129*, e2023JG007672. [CrossRef]

Disclaimer/Publisher's Note: The statements, opinions and data contained in all publications are solely those of the individual author(s) and contributor(s) and not of MDPI and/or the editor(s). MDPI and/or the editor(s) disclaim responsibility for any injury to people or property resulting from any ideas, methods, instructions or products referred to in the content.